Solutocapillary instabilities in liquid bridges

L. Martin Witkowski[a] and J. S. Walker[b]
Department of Mechanical and Industrial Engineering, University of Illinois, 1206 West Green Street, Urbana, Illinois 61801

(Received 29 November 2001; accepted 2 May 2002; published 20 June 2002)

The stability of a steady, axisymmetric flow driven by a surface-tension variation due to a solute-concentration gradient is studied with a linear analysis. There is a liquid bridge with a cylindrical free surface between two collinear solid cylinders with the same radius. One cylinder injects the solute into the liquid as it melts at a velocity V_g^*, and the other cylinder preferentially absorbs the solute from the liquid as it solidifies at the same velocity. The surface tension of the free surface is assumed to be a linear function of the solute concentration. For given values of the Schmidt number Sc and of V_g^*, the first instability is a Hopf bifurcation at a critical value of a solutal Marangoni number. The present problem is related to the thermocapillary convection in the half-zone problem for which the geometry is the same, the two solids are isothermal at different temperatures and the surface tension is a linear function of temperature. Differences arise because the solute concentration distribution here is different from the temperature distribution in the half-zone problem, and V_g^* is the variable which controls these differences. Results are presented for a range of values of V_g^* for two aspect ratios and for $\mathrm{Sc}=0.5-20$. © *2002 American Institute of Physics.* [DOI: 10.1063/1.1488598]

I. INTRODUCTION

In the floating-zone crystal-growth process, a body of molten semiconductor is held by surface tension between the melting end of a cylindrical feed rod and the solidifying end of a collinear cylindrical crystal, as described by Keller *et al.*[1] The quality of the crystal depends on the liquid flow during crystal growth, and many phenomena affect the flow. Some modeling studies, such as that by Ratnieks *et al.*,[2] have included all the coupled phenomena with realistic geometries. Other modeling studies have used simplified geometries to thoroughly study a single phenomenon without the complex couplings of the actual process. The half-zone problem is a common simplified model used to study the stability of the thermocapillary convection driven by the surface-tension variation due to the temperature variation along the free surface. In the half-zone problem, the liquid is bounded by a constant-radius, cylindrical free surface and by two planar, solid, isothermal disks at different temperatures, and the surface tension is assumed to vary linearly with temperature. In the actual floating-zone process, the free-surface temperature decreases from a maximum at some intermediate circumference to the solidification temperature at the peripheries of both the feed rod and the crystal, so that the half-zone problem roughly models the thermocapillary convection between the hottest circumference and either liquid–solid interface. Half-zone thermocapillary studies have been reviewed by Kuhlmann *et al.*[3] and generalize the fundamental instability mechanisms analysis in infinite layers studied in pioneering works by Smith *et al.*[4] and Xu *et al.*[5]

There are many important uses for solid-solution crystals, such as one with 95% germanium (solvent) and 5% silicon (solute), or GeSi. The surface tension of liquid semiconductor mixtures often depends strongly on the solute concentration. Concentration gradients arise during the floating-zone growth of solid-solution crystals because the solute is either rejected into the liquid or is preferentially absorbed into the crystal during solidification. For our GeSi example, silicon is preferentially absorbed into the crystal, creating a silicon-depleted, germanium-rich region in the liquid adjacent to the crystal-growth interface. The solutocapillary convection due to the solute-concentration dependence of the surface tension is coupled to the thermocapillary convection, buoyant convection, etc., for the actual floating-zone growth of solid-solution crystals, but our objective is to study the stability of solutocapillary convection without the complex couplings of the actual process.

Relatively few publications have focused on solutocapillary convection with or without thermocapillary convection. Kaddeche *et al.*[6] presented numerical solutions for the coupled solutocapillary and thermocapillary convections in a rectangular geometry with a top free surface in order to model the horizontal Bridgman crystal-growth process. Schwabe *et al.*[7] presented an experimental study of coupled thermocapillary and solutocapillary convections during the transient solidification of a liquid bridge, where the solutocapillary convection arose from a surfactant. Two important numerical models considered solutocapillary convection in a

[a]Present address: LIMSI-CNRS, BP 133, F91403 Orsay Cedex, France; electronic mail: witko@limsi.fr
[b]Electronic mail: jswalker@uiuc.edu

cylindrical geometry[8] and a planar geometry.[9] In both models there was no solute transport across the liquid–solid interfaces, while here we emphasize the roles of solute injection at the melting interface and the preferential solute absorption at the solidifying interface. Campbell *et al.*[10] presented experimental results for the floating-zone growth of GeSi crystals which demonstrated that the solutocapillary convection can overwhelm the thermocapillary convection, leading to a reversal of the direction of the circulation near the crystal-growth interface. This paper presents a linear stability analysis for the solutocapillary convection in a liquid bridge between a melting feed rod and a solidifying crystal. Actual processes involve couplings and geometric complexities which are ignored here because an understanding of instabilities of the solutocapillary convection alone is needed before treating the complex couplings of the actual process. Our primary objective is to compare and contrast our idealized study of solutocapillary instabilities with the idealized half-zone studies of thermocapillary instabilities. The differences arise primarily from the differences between the basic temperature variation in the half-zone problem and the basic solute concentration variation in the present problem. In the half-zone problem, the axial temperature variation without thermocapillary convection is linear, but in the present problem the axial variation of the solute concentration without solutocapillary convection depends on V_g^*, i.e., the velocity at which the feed rod melts and the crystal grows. We consider the preferential absorption of the solute into the crystal, but the results are equally valid for solute rejection into the liquid. Preferential solute absorption into the crystal produces a solute-depleted region near the crystal-growth interface, and this leads to diffusion of the solute entering at the melting interface toward the crystal-growth interface. If V_g^* is large, then the melting liquid keeps its original solute concentration until it is relatively close to the crystal-growth interface when the solute concentration begins to decrease due to diffusion across a mass-diffusion boundary layer adjacent to this interface. On the other hand, if V_g^* is small, diffusion dominates over convective mass transport with V_g^*, so that the solute entering the liquid at the melting interface is immediately depleted by diffusion toward the crystal-growth interface. Thus V_g^* is a key variable for our solutocapillary convection, and it has no counterpart in the half-zone thermocapillary problem. The effects of varying V_g^* are the primary focus of this paper. The temperature difference along the free surface in the half-zone problem is fixed, but the solute concentration along the free surface in our problem is a result which strong depends on V_g^*. Therefore we initially use the solute concentration in the feed rod to normalize variables, and finish by rescaling the results with the dimensionless solute concentration difference along the free surface in order to make meaningful comparisons with the thermocapillary instability in the half-zone problem.

II. PROBLEM FORMULATION

A. General formulation

We model the float-zone process as a liquid bridge with a cylindrical free surface at a constant radius R^* and with two plane liquid–solid interfaces at a distance of $2bR^*$ from each other. The geometry is sketched in Fig. 1. We normalize all geometrical quantities by R^* and use cylindrical coordinates r,θ,z with the z axis along the centerline of the cylinder with the origin at the middle of the liquid region and with unit vectors $\mathbf{e}_r,\mathbf{e}_\theta,\mathbf{e}_z$. The velocities, pressure, concentration, and time are normalized by ν/R^*, $\rho\nu^2/R^{*2}$, C_f^*, and R^{*2}/ν where ν, ρ, and C_f^* are the kinematic viscosity, density, and concentration of the feed rod.

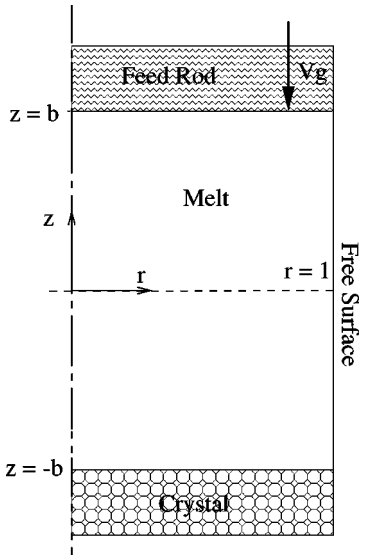

FIG. 1. Geometry with lengths normalized by R^*.

The dimensionless equations governing momentum and concentration of the solute in the liquid are

$$\frac{\partial \mathbf{V}'}{\partial t}+((\mathbf{V}'-V_g\mathbf{e}_z)\cdot\boldsymbol{\nabla})\mathbf{V}'=-\boldsymbol{\nabla}P'+\nabla^2\mathbf{V}', \tag{1}$$

$$\boldsymbol{\nabla}\cdot\mathbf{V}'=0, \tag{2}$$

$$\frac{\partial C'}{\partial t}+((\mathbf{V}'-V_g\mathbf{e}_z)\cdot\boldsymbol{\nabla})C'=\frac{1}{\mathrm{Sc}}\nabla^2C', \tag{3}$$

where $\mathbf{V}'$, C', P', and t are the velocity, concentration of the solute, pressure, and time. The dimensionless parameters are the crystal-growth Reynolds and Schmidt numbers, defined as

$$V_g=\frac{V_g^*R^*}{\nu},\quad \mathrm{Sc}=\frac{\nu}{D},$$

where D is the diffusion coefficient for the solute in the solvent.

The boundary conditions for the liquid–solid interfaces are

$$\mathbf{V}'=0,\quad \frac{\partial C'}{\partial z}+V_g\,\mathrm{Sc}(1-k_s)C'=0 \qquad \text{at} \quad z=-b, \tag{4}$$

$$\mathbf{V}'=0,\quad \frac{\partial C'}{\partial z}-V_g\,\mathrm{Sc}(1-C')=0 \qquad \text{at} \quad z=b, \tag{5}$$

where k_s is the segregation coefficient. Some background information on the segregation mechanisms can be found in Garandet *et al.*[11] The boundary conditions for the free surface at $r=1$ are

$$V_r'=0, \quad \frac{\partial V_z'}{\partial r}-\frac{\mathrm{Ma}}{\mathrm{Sc}}\frac{\partial C'}{\partial z}=0, \quad \frac{\partial V_\theta'}{\partial r}-V_\theta'-\frac{\mathrm{Ma}}{\mathrm{Sc}}\frac{\partial C'}{\partial \theta}=0, \quad \frac{\partial C'}{\partial r}=0, \tag{6}$$

where Ma is the solutal Marangoni number, defined as

$$\mathrm{Ma}=\frac{|d\gamma/dC^*|C_f^*R^*}{D\nu}.$$

In order to study the linearized equation near the critical value, we write the velocity in the following form:

$$\mathbf{V}'(r,\theta,z,t)=\mathbf{V}(r,z)+\epsilon \ \ \mathrm{Real}[\mathbf{v}(r,\theta,z,t)]. \tag{7}$$

Here ϵ is a small parameter and $\mathbf{v}(r,\theta,z,t)$ is a superposition of complex normal modes

$$(v_r(r,z),iv_\theta(r,z),v_z(r,z))\exp(\lambda t+im\theta), \tag{8}$$

where m is the azimuthal wave number, $\lambda=\lambda_r+i\lambda_i$ with the growth rate λ_r and the oscillation frequency λ_i. A similar formulation is used for $P'(r,\theta,z,t)$ and $C'(r,\theta,z,t)$.

B. Basic state

We use a stream-function (ψ), vorticity (Ω) formulation to compute the velocity field $\mathbf{V}(r,z)=V_r\mathbf{e}_r+V_z\mathbf{e}_z$ with the following definition:

$$V_r=\frac{1}{r}\frac{\partial\psi}{\partial z}, \quad V_z=-\frac{1}{r}\frac{\partial\psi}{\partial r}, \quad \Omega=\frac{\partial V_r}{\partial z}-\frac{\partial V_z}{\partial r}$$

so that the Navier–Stokes equations reduce to

$$\frac{\partial(V_r\Omega)}{\partial r}+\frac{\partial((V_z-V_g)\Omega)}{\partial z}=\frac{\partial^2\Omega}{\partial r^2}+\frac{1}{r}\frac{\partial\Omega}{\partial r}-\frac{\Omega}{r^2}+\frac{\partial^2\Omega}{\partial z^2}, \tag{9}$$

$$\frac{\partial^2\psi}{\partial r^2}-\frac{1}{r}\frac{\partial\psi}{\partial r}+\frac{\partial^2\psi}{\partial z^2}=r\Omega, \tag{10}$$

and the equation governing the basic state concentration is

$$\frac{\partial(V_rC)}{\partial r}+\frac{V_rC}{r}+\frac{\partial((V_z-V_g)C)}{\partial z}=\frac{1}{\mathrm{Sc}}\left(\frac{\partial^2C}{\partial r^2}+\frac{1}{r}\frac{\partial C}{\partial r}+\frac{\partial^2C}{\partial z^2}\right). \tag{11}$$

The symmetry conditions at $r=0$ are $\psi=\Omega=\partial C/\partial r=0$. The boundary conditions at $z=b$ are $\psi=\partial\psi/\partial z=0$, $\partial C/\partial z=V_g\,\mathrm{Sc}(1-C)$, at $z=-b$ are $\psi=\partial\psi/\partial z=0$, $\partial C/\partial z=-V_g\,\mathrm{Sc}(1-k_s)C$, and at $r=1$ are $\psi=\partial C/\partial r=0$, $\Omega=-(\mathrm{Ma}/\mathrm{Sc})f_z(\partial C/\partial z)$, where $f_z=1-\exp(-\alpha(1-(z/b)^2)^2)$ (α being an arbitrary parameter) is a regularization function introduced to remove the singularity in the corner region. This procedure is similar to the one used by Wanschura *et al.*[12] or Chénier *et al.*[13] and has been discussed in detail by Canright[14] and Kasperski *et al.*[15]

The set of equations and boundary conditions are discretized by a standard second-order accurate centered finite difference scheme on a uniform grid. The Neumann boundary condition for ψ is not computed explicitly but used in the formulation for the vorticity on the solid boundary where we used the Thom formula. As an example, for the top wall: $r_i\Omega_{i,w}=2\psi_{i,w-1}/(\Delta z)^2$ where the subscript i is the index for the radial grid, w is the index for the wall, and Δz the axial mesh size. The steady state solutions are computed using a Newton–Raphson algorithm.[16] The unknowns are properly ordered on each node to form a banded matrix. At each Newton–Raphson iteration, the matrix inversion is done by the routines dgbtrf/dgbtrs taken from the LAPACK library.[17]

C. Linear stability

The linear stability equations are obtained by introducing Eq. (7) in Eqs. (1)–(6) and collecting all terms of order ϵ. We obtain from the Navier–Stokes equations,

$$\frac{2}{r}\frac{\partial}{\partial r}(rv_rV_r)-m\frac{v_\theta V_r}{r}+\frac{\partial}{\partial z}(v_r(V_z-V_g))+\frac{\partial}{\partial z}(v_zV_r)+\frac{\partial p}{\partial r}-\left(\frac{\partial^2v_r}{\partial r^2}+\frac{1}{r}\frac{\partial v_r}{\partial r}-\frac{(1+m^2)v_r}{r^2}+\frac{2mv_\theta}{r^2}+\frac{\partial^2v_r}{\partial z^2}\right)=-\lambda v_r, \tag{12}$$

$$\frac{1}{r}\frac{\partial}{\partial r}(rv_\theta V_r)+\frac{\partial}{\partial z}(v_\theta(V_z-V_g))+\frac{v_\theta V_r}{r}+\frac{mp}{r}-\left(\frac{\partial^2v_\theta}{\partial r^2}+\frac{1}{r}\frac{\partial v_\theta}{\partial r}-\frac{(1+m^2)v_\theta}{r^2}+\frac{2mv_r}{r^2}+\frac{\partial^2v_\theta}{\partial z^2}\right)=-\lambda v_\theta, \tag{13}$$

$$\frac{1}{r}\frac{\partial}{\partial r}(rv_r(V_z-V_g))+\frac{1}{r}\frac{\partial}{\partial r}(rV_rv_z)-m\frac{v_\theta(V_z-V_g)}{r}+2\frac{\partial}{\partial z}(v_z(V_z-V_g))+\frac{\partial p}{\partial z}-\left(\frac{\partial^2v_z}{\partial r^2}+\frac{1}{r}\frac{\partial v_z}{\partial r}-\frac{m^2v_z}{r^2}+\frac{\partial^2v_z}{\partial z^2}\right)=-\lambda v_z, \tag{14}$$

$$\frac{1}{r}\frac{\partial(rv_r)}{\partial r}-m\frac{v_\theta}{r}+\frac{\partial v_z}{\partial z}=0, \tag{15}$$

and from the equation governing the concentration of the solute in the liquid

$$\frac{1}{r}\frac{\partial(rcV_r)}{\partial r}+\frac{1}{r}\frac{\partial(rv_rC)}{\partial r}+\frac{\partial(c(V_z-V_g))}{\partial z}+\frac{\partial(v_zC)}{\partial z}-\frac{1}{\mathrm{Sc}}\left(\frac{\partial^2c}{\partial r^2}+\frac{1}{r}\frac{\partial c}{\partial r}-\frac{m^2c}{r^2}+\frac{\partial^2c}{\partial z^2}\right)=-\lambda c. \tag{16}$$

TABLE I. Comparison of $\psi_{\max}$ for various grid sizes and regularization functions. "no cv" means no convergence could be reached in the Newton iterative process. "Shen reg" is a fairly smooth regularization as described on page 920 of Wanschura *et al.* (Ref. 12). "Spect meth" is an independent code we developed using Chebyshev polynomials with 24 and 30 collocation points in the radial and axial directions, respectively.

Ma=	400	2000	4000	12 000	20 000	28 000	Grid size or Ref.
$\psi_{\max}$=	0.5751	no cv	no cv	no cv	no cv	no cv	40×40; $f_z=1$
$\psi_{\max}$=	0.5821	1.455	no cv	no cv	no cv	no cv	80×80; $f_z=1$
$\psi_{\max}$=	0.5819	1.456	2.317	no cv	no cv	no cv	80×80; $\alpha=150$
$\psi_{\max}$=	0.5808	1.447	2.296	6.302	no cv	no cv	80×80; $\alpha=50$
$\psi_{\max}$=	0.577	1.416	2.220	6.047	10.23	14.54	80×80; Shen reg.
$\psi_{\max}$=	0.5837	1.466	2.326	6.195	10.01	13.78	160×160; $\alpha=150$
$\psi_{\max}$=	0.5841	1.468	2.333	6.159	9.864	13.59	Spect meth $\alpha=150$
$\psi_{\max}$=			2.33	6.15	9.75	13.16	Ref. 20 (Wanschura)
$\psi_{\max}$=			2.35	6.27	9.85	13.02	Ref. 20 (Leypoldt)

The symmetry conditions at $r=0$ are: $v_r=v_\theta=v_z=c=0$ for $m>1$ and $\partial v_r/\partial r=\partial v_\theta/\partial r=v_z=c=0$ for $m=1$. The boundary conditions are $v_r=0, \partial v_\theta/\partial r=(\mathrm{Ma/Sc})f_z mc$, $\partial v_z/\partial r=(\mathrm{Ma/Sc})f_z(\partial c/\partial z)$, $\partial c/\partial r=0$, at the free surface; $v_r=0$, $v_\theta=0$, $v_z=0$, $\partial c/\partial z=-V_g\,\mathrm{Sc}\,c$ at the melting front and $v_r=0$, $v_\theta=0$, $v_z=0$, $\partial c/\partial z=V_g\,\mathrm{Sc}\,(k_s-1)\,c$ at the solidification front.

As for the basic state, the equations and boundary conditions are discretized with finite differences. The unknowns are computed on the same grid points used for the basic flow with the exception of the pressure that is located at the center of the cell. The choice of this scheme, sometimes called 4/1 staggered grid or semi-staggered grid scheme is similar to the one chosen by Chen *et al.*[16] and is used mainly for its simplicity. More details and comparisons with various other schemes can be found in Shih *et al.*[18] The continuity equation is solved by a modified penalty function method, namely Eq. (15) is modified to

$$\frac{1}{r}\frac{\partial(rv_r)}{\partial r}-m\frac{v_\theta}{r}+\frac{\partial v_z}{\partial z}=\epsilon_p p, \tag{17}$$

where ϵ_p is a small arbitrary constant. For all the calculations presented here, we found that $\epsilon_p=10^{-8}$ was adequate to ensure that the error in the continuity equation was of the same order of magnitude as that associated with the second-order accurate scheme.

The resulting discrete forms of Eqs. (12)–(14), (16) and (17) and the associated boundary conditions lead to a generalized eigenvalue problem. The search for the leading eigenvalues, i.e., those with the largest real part is performed with the help of the shift-invert spectral transformation method implemented in ARPACK library.[19] We wrote a modified version of the corresponding driver zndrv4.

The procedure to find the critical Ma value, all other parameters being fixed, is an iterative zero search for λ_r with the following steps: (i) the basic flow with a guessed Ma is computed by Newton's method, (ii) the largest real part eigenvalue is found by ARPACK, (iii) the next guess for Ma is computed by a secant method. This procedure converges usually within five or six iterations provided that the two initial guesses needed by the secant method are reasonably close to the solution.

III. RESULTS

A. Validation procedure

In order to validate the general procedure, we did a slight modification to the original code so that we can compare our results with those obtained for the half-zone problem which is a benchmark for thermocapillary instabilities. We set $V_g=0$, $C(r,\pm 0.5)=\mp 0.5$ and $c(r,\pm 0.5)=0$. Also, in order to have a positive value for Ma, we changed its sign in the boundary conditions at the free surface. Our problem then corresponds to the half-zone thermocapillary problem with C and Sc representing the temperature and the Prandtl number Pr, respectively.

As in practice the Schmidt number is large, we focus on comparisons with Sc=4 for which detailed results can be found in previous studies.[12,16,20] We compare the maximum value of the stream function in Table I for various grid sizes and for various regularization functions with the values found in Table I of Leypoldt *et al.*[20]

The regularization function for the spectral method is needed because of the singularity in the corner,[12] but the results in Table I also illustrate the need for a regularization function for the finite-difference method if there is a lack of resolution of the large temperature gradient in the corner region. The effect of the regularization function is noticeable on the maximum value of ψ, and more pronounced effects would be expected in values of the velocities close to the corners.[15] Nevertheless, these variations on the base flow have little effect on Ma_c, the critical values of Ma. We found on both a coarse grid with a smooth regularization and a fine grid with a stiff regularization that $m=2$ is the critical mode. For the coarse 41×41 grid, $\mathrm{Ma}_c=4177$ with $\lambda_i=28.3$ using "Shen reguralization" and for the finer 81×81 grid with $\alpha=150$, $\mathrm{Ma}_c=4028$ with $\lambda_i=28.3$. There is satisfactory agreement with the values of $\mathrm{Ma}_c=4188$ with $\lambda_i=27.9$ found by Wanschura *et al.*[12] and of $\mathrm{Ma}_c=3980$ with $\lambda_i=28.3$ found by Chen *et al.*[16] The lack of variation of Ma_c with changes in accuracy for the base flow is surprising. This lack of variation appears to arise from the fact that the key elements in the instability are the large gradients of velocity and temperature near the middle of the free surface, which

TABLE II. Critical Marangoni number, dimensionless concentration difference along the free surface, effective Marangoni number, Hopf frequency, critical mode, and maximum of the stream function for $b=0.5$ and Sc $=4$ for various values of V_g.

V_g	Ma_c	ΔC	$\mathrm{Ma}_{\mathrm{eff}}$	λ_i	m	$\psi_{\max}$
0.01	3.81×10^{5}	5.01×10^{-3}	1907	25.4	2	1.749
0.1	4.19×10^{4}	4.74×10^{-2}	1985	25.9	2	1.798
0.5	1.17×10^{4}	0.194	2277	28.0	2	1.963
1.0	8185	0.319	2614	30.3	2	2.129
2.0	7075	0.471	3333	34.5	2	2.446
3.0	7390	0.558	4125	38.6	2	2.782
4.0	7635	0.621	4744	47.4	3	2.989

are not affected by the boundary layers at the solid interfaces.

For Sc$=0.5$, the critical mode and the critical Marangoni value are more controversial. Wanschura *et al.*[12] found $\mathrm{Ma}_c=5126$ with $\lambda_i=245.5$ for $m=2$ while Chen *et al.*[16] found $\mathrm{Ma}_c=4516.5$ with $\lambda_i=250.2$ for $m=3$. Our calculations on a 81×81 grid with $\alpha=50$, showed that $m=3$ is the critical mode for $\mathrm{Ma}_c=4857$ with $\lambda_i=252.5$.

Some comparisons for Sc$=0.02$ were also done and for this low value of Sc the agreement was excellent for the base flow as well as for the critical value of the Marangoni number. In this case, the bifurcation is stationary with $\lambda_i=0$ and the critical mode is $m=2$. We found that $\mathrm{Ma}_c=41.09$ on a 81×81 grid with no regularization. Chen *et al.* found $\mathrm{Ma}_c=41.08$ and Wanschura *et al.*[12] found $\mathrm{Ma}_c=41.24$.

B. Variation with V_g for $b=0.5$ and Sc$=4$

In order to relate our results to those obtained for the half-zone thermocapillary problem, we set Sc$=4$ and $b=0.5$. The value of the segregation coefficient $k_s=4.2$ is chosen to correspond with the experiments of Campbell *et al.*[10] We choose $\alpha=50$ and a 101×101 grid. We give a short comment on this point at the end of this section.

When the value of V_g is small, where $V_g\sim0.02$ would be a typical value for alloyed crystal growth, the concentration gradients of the solute in the melt are small. The axial distribution of concentration can be roughly estimated by the one-dimensional model for $\mathbf{V}=0$ so that C is only a function of z. In such case,

$$C_{1-d}(z)=1-\frac{k_s-1}{k_s}\exp(-V_g\,\mathrm{Sc}(z+b)). \tag{18}$$

For $V_g\,\mathrm{Sc}\ll1$, the concentration difference $\Delta C_{1-d}=C_{1-d}(b)-C_{1-d}(-b)\sim2bV_g\,\mathrm{Sc}(k_s-1)/k_s$ which is small. For $V_g=0.01$, $\Delta C_{1-d}=0.030$. This estimate is good as long as the velocity in the melt is small enough. For Ma $=10^3,10^4$ and the critical Marangoni $\mathrm{Ma}_c=3.81\times10^5$, we find that $\Delta C=C(1,b)-C(1,-b)=0.029,0.018$, and 0.0050, respectively. Our Marangoni number is based on the feed rod concentration C_f^* rather than on a concentration difference along the free surface. Since the dimensionless temperature difference along the free surface is one for the half-zone problem, we introduce an effective Marangoni $\mathrm{Ma}_{\mathrm{eff}}=\mathrm{Ma}_c\Delta C$ which can only be computed *a posteriori*, but which can be compared to the Ma for thermocapillary instabilities to reveal the effects of V_g. Thus when V_g is small, the critical value of $\mathrm{Ma}_{\mathrm{eff}}$ is very close to the Ma_c found in the thermocapillary case. The critical Marangoni numbers and their associated modes can be found in Table II. The base state velocity field consists of a single torus similar to the one for thermocapillary convection. At the free surface, there is a strong flow convecting liquid with low concentra-

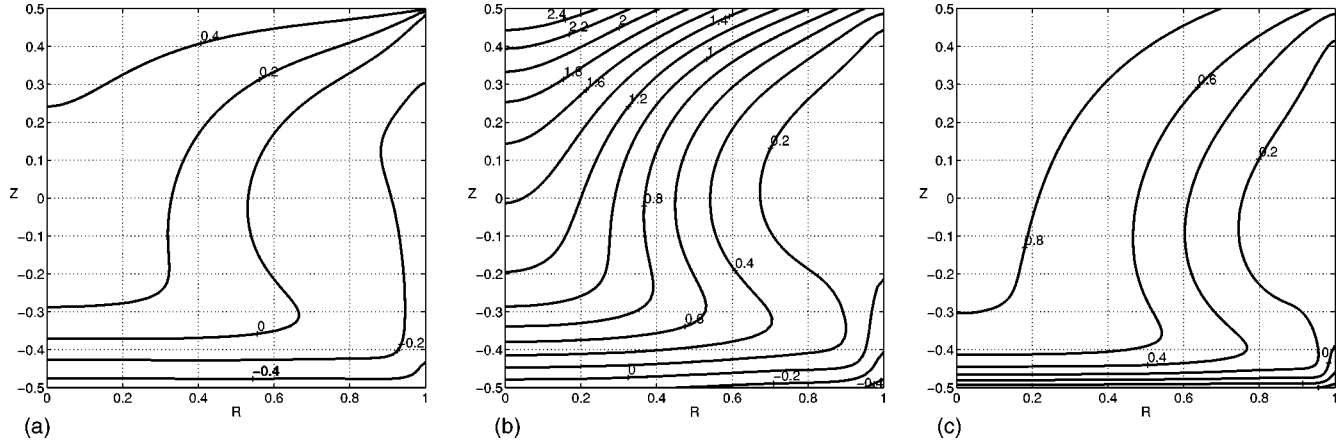

FIG. 2. Contours plots of C when $\mathrm{Ma}=\mathrm{Ma}_c$. (a) C for Ma$=4028$ (thermocapillary half-zone configuration); (b) C_{res} for $V_g=0.1$; (c) C_{res} for $V_g=4.0$.

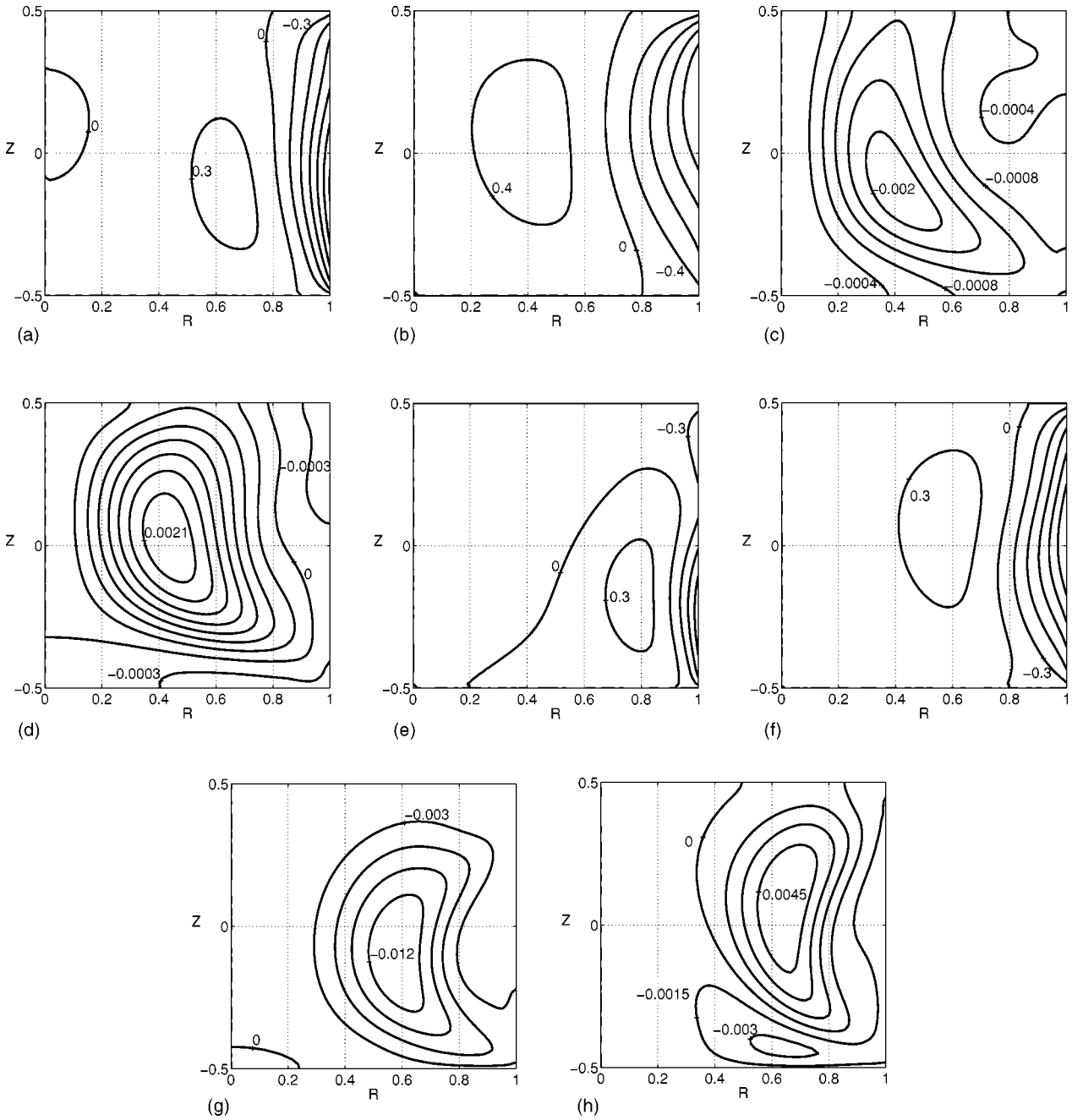

FIG. 3. Contours plots of the real and imaginary part of v_θ and c when $\mathrm{Ma}=\mathrm{Ma}_c$. From left to right and top to bottom: (a) $v_{\theta r}$ for $V_g=0.1$; (b) $v_{\theta i}$ for $V_g=0.1$; (c) c_r for $V_g=0.1$; (d) c_i for $V_g=0.1$; (e) $v_{\theta r}$ for $V_g=4$; (f) $v_{\theta i}$ for $V_g=4$; (g) c_r for $V_g=4$; (h) c_i for $V_g=4$.

tion toward the feed rod. The maximum value of the stream function is given in Table II. The lines of constant concentration are represented in Fig. 2. In Fig. 2, we rescaled the concentration so that $C_{\mathrm{res}}=(C-C(1,-b))/\Delta C-0.5$. The rescaling has two goals: first to be able to compare the distribution of concentration with the temperature distribution for the half-zone problem in Fig. 2(a), and second to be able to compare the concentration distribution as V_g varies. Once rescaled, the concentration distribution is almost identical for $V_g=0.1$ and $V_g=0.01$ (not represented here), which indicates a V_g independent regime for $V_g \ll 1$ at the bifurcation point. This is emphasized by the small changes in the value of $\mathrm{Ma}_{\mathrm{eff}}$. When V_g gets larger [see Fig. 2(c)], a boundary layer develops along the solidification front at $z=-b$ and a constant concentration central core region appears. The radial concentration gradient due to the convection by the flow moves closer to the free surface and down toward the solidification front. We always found the first transition to be an Hopf bifurcation, where the mechanism is similar to a hydrothermal wave requiring both a radial concentration gradient at the free surface and inertial effects for instability (see Wanschura *et al.*[12] for more details). We present in Fig. 3 the perturbed azimuthal velocity and concentration for $V_g=0.1$ and 4. The perturbation is normalized so that $v_z(1,0)=10$. As V_g is increased, the critical mode is changed from $m=2$ to $m=3$. This change can be explained by the fact that

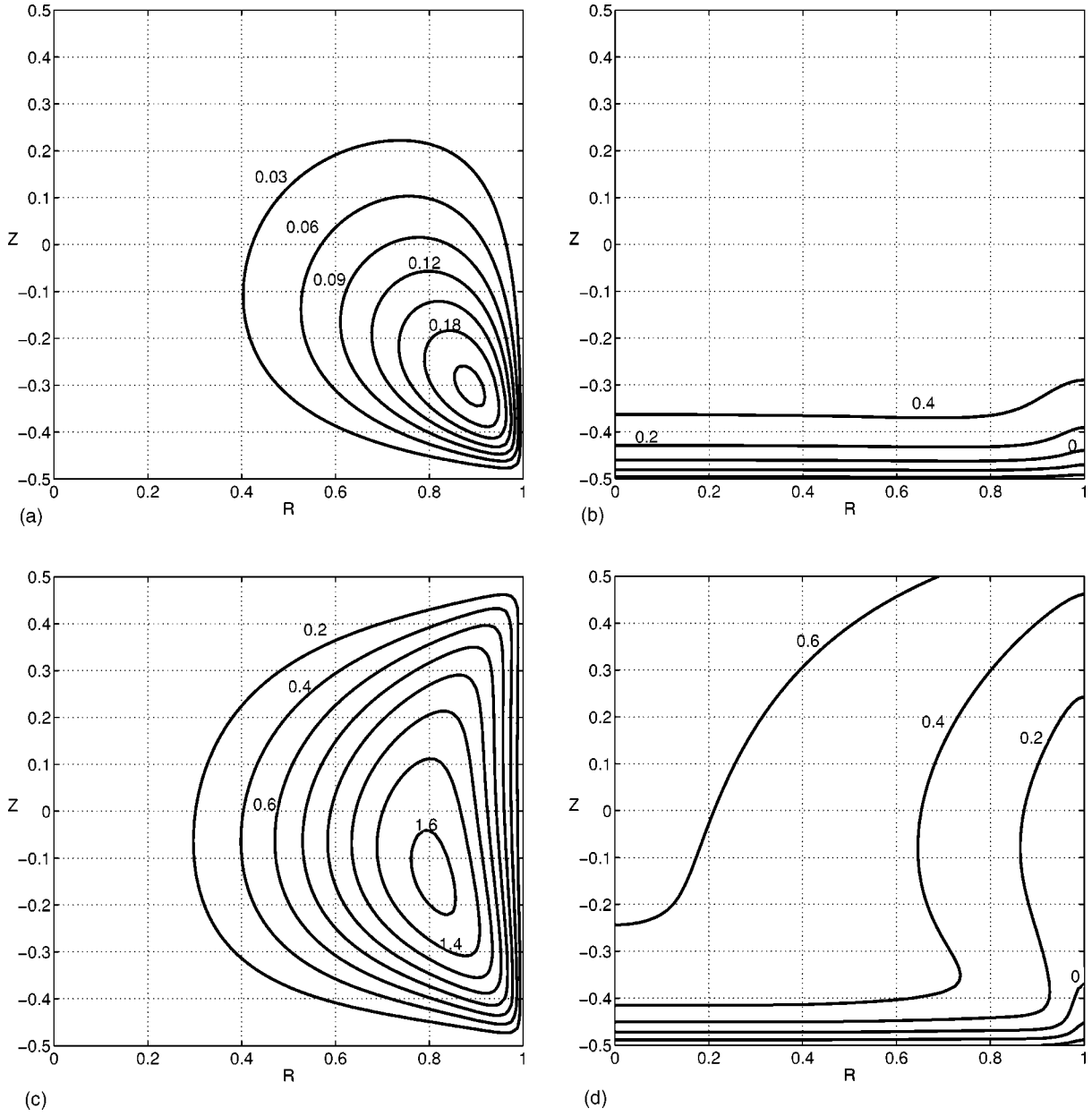

FIG. 4. Contours plots when $V_g=4$ of (a) ψ for Ma=250; (b) C_{res} for Ma=250; (c) ψ for Ma=2500; (d) C_{res} for Ma=2500.

for small V_g the only scales are the radius and the height. In the half-zone problem, the critical mode depends on the aspect ratio b. As b gets small, the critical mode m increases, as well as the critical Marangoni number. This result holds for small values of Pr[12,16] and for large values of Pr.[21] In the solutocapillary problem for large value of V_g another scaling emerges, namely the thickness of the solutal boundary layer that varies as $(V_g\,\mathrm{Sc})^{-1}$ for $V_g\,\mathrm{Sc}\gg 1$. Thus large values of V_g effectively reduce the axial scale of key phenomenon, leading to larger m for the critical mode.

TABLE III. Grid size and regularization influence on Ma_c and $\psi_{\max}$ for $V_g=4$ and $m=3$.

$nr\times nz$	α	Ma_c	$\psi_{\max}$
41×41	50	5664	3.253
61×61	50	6565	3.088
101×101	50	7635	2.989
101×101	20	8011	3.035
101×101	100	7469	2.974
141×141	50	8027	2.970

TABLE IV. Critical Marangoni number, concentration difference along the free surface, effective Marangoni number, Hopf frequency, critical mode, and maximum of the stream function for $b=1$ and Sc=4.

V_g	Ma_c	ΔC	Ma_{eff}	λ_i	m	$\psi_{\max}$
0.01	1.21×10^{5}	9.27×10^{-3}	1117	9.66	1	1.226
0.1	1.35×10^{4}	8.58×10^{-2}	1156	9.85	1	1.258
0.5	4134	0.322	1332	10.6	1	1.386
1.0	3118	0.492	1535	11.4	1	1.511
2.0	3006	0.658	1977	12.9	1	1.738
3.0	3375	0.731	2468	14.3	1	1.948
4.0	3902	0.770	3002	15.6	1	2.144
5.0	4519	0.791	3576	16.9	1	2.330
6.0	4969	0.807	4010	26.2	2	2.454

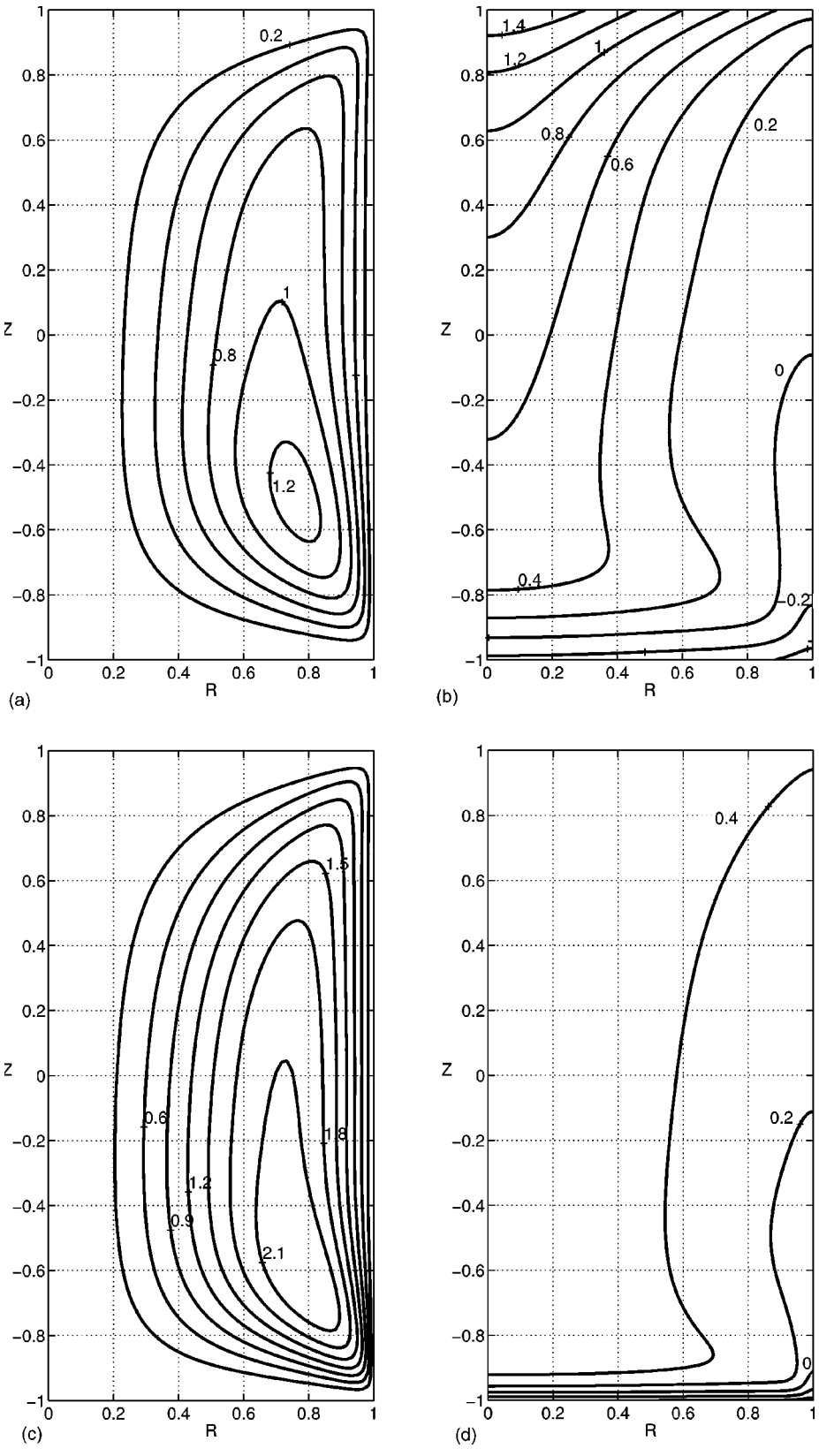

FIG. 5. Contours plots when Ma $=\mathrm{Ma}_c$ of (a) ψ for $V_g=0.1$; (b) C_{res} for $V_g=0.1$; (c) ψ for $V_g=5.0$; (d) C_{res} for $V_g=5.0$.

For large V_g, if we increase Ma from 0 to Ma_c we see that for low Ma the flow is weak and confined close to $r=1, z=-b$. Then as Ma increases, the velocity increases so that the low concentration is convected along the free surface leading to a radial concentration gradient. This is illustrated in Fig. 4 where we present the base flow and concentration distribution for two values of Ma smaller than Ma_c. At Ma_c, the toroidal circulation expands to the entire cavity to the point where inertia and the radial concentration gradient are strong enough to trigger a hydrosolutal wave.

We now make a brief comment on grid size and regularization. As V_g gets large, the resolution needs to be in-

creased. The challenge is to resolve the solutal boundary layer for the basic state. We made some grid dependence and regularization tests to confirm the choice of a 101×101 grid and $\alpha=50$. In Table III, we present the results for a large value of V_g, which is the most computationally challenging situation. The sensitivity to the regularization is still moderate. The same tests have been done for $V_g=0.1$ and showed an overall variation of only 3% over the entire range of grid size and regularization.

C. Variation with V_g for $b=1$ and Sc=4

The aspect ratio $b=0.5$ studied in Sec. III B allowed us to compare the soluto capillary flow with the thermocapillary flow for the half-zone configuration which has been designed to represent half the domain of the crystal growth process where $b=1$. For the solutocapillary convection with $b=1$, we keep the other parameter to be the same, namely Sc=4 and $k_s=4.2$. We also set the regularization factor $\alpha=50$ and used a 101×201 grid. The critical Marangoni numbers and the associated modes can be found in Table IV for various values of V_g. To illlustrate, the base state, we present in Fig. 5 the streamlines and the lines of constant concentration for a small and a large value of V_g. The concentration is rescaled in the same way as that described in Sec. III B. The V_g independent regime for $V_g\ll1$ at the bifurcation point is also valid for this aspect ratio so that the results for $V_g=0.01$ and $V_g=0.1$ are almost identical after rescaling.

We notice that as V_g increases, the eye of the circulation gets closer to $r=1$, $z=-b$ and a strong jet is produced at the free surface. A regime at large V_g for which the aspect ratio no longer plays a role due to the presence of the length scale imposed by the solutal layer is not reached for $b=1$ and $V_g=6$. The recirculation is still present in most of the cell even if the solutal layer is approximately 1/20 of the axial length. At the transition, the inertia is always strong enough so that with the stress free boundary condition at $r=1$, the jet produced by the driving force close to $z=-b$ is not damped until it reaches $z=b$. Thus even if the base flow is governed by the solutal layer, the nature of the instability is similar to that for the half-zone aspect ratio. The transition goes through a Hopf bifurcation and an hydrosolutal wave propagates in the azimuthal direction. When V_g increases, the critical mode changes from $m=1$ to $m=2$ for similar reasons as for $b=0.5$.

D. Variation with Sc for $b=1$ and $V_g=0.1$

In the experiments of Campbell *et al.*,[10] the value of Sc is in the range of 10–20. We study the influence of Sc for $V_g=0.1$. As Sc is increased from 0.5 to 20, the rescaled concentration does not change significantly, and the lines of constant concentration are very similar to those presented in Fig. 5(b). As can be seen in Table V, $\psi_{\max}$ is a decreasing function of Sc while $\mathrm{Ma}_{\mathrm{eff}}$ increases. The major effect of varying Sc can be found in the phase shift between the perturbed azimuthal velocity and concentration. We present in Table V, the phase shift

TABLE V. Critical Marangoni number, concentration difference along the free surface, effective Marangoni number, Hopf frequency, critical mode, maximum of the stream function, and the phase shift for $b=1$, $V_g=0.1$, and various Sc.

Sc	Ma_c ($\times10^4$)	ΔC	$\mathrm{Ma}_{\mathrm{eff}}$	λ_i	m	$\psi_{\max}$	$\Delta\Phi$
0.5	2.84	1.88×10^{-2}	533.9	26.1	1	6.560	0.219
1	2.24	3.11×10^{-2}	696.9	19.6	1	3.867	0.190
2	1.70	5.21×10^{-2}	886.3	14.1	1	2.192	0.176
4	1.35	8.58×10^{-2}	1156	9.85	1	1.258	0.149
8	1.27	0.132	1682	6.86	1	0.7719	0.105
12	1.44	0.162	2322	5.60	1	0.6151	0.074
16	1.70	0.182	3096	4.86	1	0.5421	0.051
20	1.99	0.199	3948	4.33	1	0.4993	0.031

$$\Delta\Phi=\arctan\left(\frac{v_{\theta i}(1,0)}{v_{\theta r}(1,0)}\right)-\arctan\left(\frac{c_i(1,0)}{c_r(1,0)}\right). \tag{19}$$

It can be noted that at low Sc, the phase shift is nearly a quarter of a period while reducing Sc further would probably lead to a stationary transition regime as in the thermocapillary case. For larger Sc, the phase shift is decreasing and seems to asymptote to a regime for which the ratio of mass diffusion to the momentum diffusion is no longer the key to control the hydrosolutal mechanism.

IV. CONCLUSIONS

We have studied the primary instability of an axisymmetric steady solutocapillary flow with respect to three-dimensionnal perturbation. We did a comparison between thermocapillary and solutocapillary configuration for the base flow and the instability patterns and mechanism. We showed that there are major differences in the base flow due to a new control parameter, the growth velocity. The latter controls the axial distribution of concentration through the boundary conditions at the solid-melt interfaces. When V_g increases the concentration gradients are not uniform along the free surface. For large values of the growth velocity, the base flow is only driven by a thin solutal layer close to the crystal-melt interface. Even for such case, the driving terms for instability are due to a large scale flow with inertia and a radial concentration gradient at the free surface. The perturbation pattern is then similar to an hydrothermal wave propagating in the azimuthal direction. For values of Sc and aspect ratios studied here, the effect of V_g is to change the azimuthal dominant mode as well as the critical Marangoni number but do not influence the nature of the instability.

From this study, we conclude that if we retain as unique driving force the gradient of surface tension due to concentration variation, the instability is not localized to regions with strong concentration gradient but leads to a large scale instability throughout the entire melt. A more complex study where both thermocapillary and solutocapillary effects are included is needed to explain the local changes close to the crystal-melt interface observed by Campbell *et al.*[10]

ACKNOWLEDGMENTS

This research was supported by the US National Aeronautics and Space Administration under Grant No. NAG 8–1453. The calculations were performed on SGI Origin 2000 at The National Center for Supercomputing Applications. The authors are indebted to G. Chen at Irphe, Marseille, France, D. Henry at Ecole Centrale de Lyon, France, and L. Tuckermann at Limsi, Paris, France for their help in the set up of the numerical techniques used in this work.

[1]W. Keller and A. Mühlbauer, *Floating-zone Silicon* (Dekker, New York, 1981).
[2]G. Ratnieks, A. Muiznieks, A. Muhlbauer, and G. Raming, ''Numerical 3D study of FZ growth: Dependence on growth parameters and melt instability,'' J. Cryst. Growth **230**, 48 (2001).
[3]H. Kuhlmann and H. J. Rath, ''Hydrodynamic instabilities in cylindrical thermocapillary liquid bridges,'' J. Fluid Mech. **247**, 247 (1993).
[4]M. K. Smith and S. H. Davis, ''Instabilities of dynamic thermocapillary liquid layers. Part 1. Convective instabilities,'' J. Fluid Mech. **132**, 119 (1983).
[5]J. J. Xu and S. H. Davis, ''Convective thermocapillary instabilities in liquid bridges,'' Phys. Fluids **27**, 1102 (1984).
[6]S. Kaddeche, H. BenHadid, and D. Henry, ''Macrosegregation and convection in the horizontal Bridgman configuration II. Concentrated alloys,'' J. Cryst. Growth **141**, 279 (1994).
[7]D. Schwabe, X. Da, and A. Scharmann, ''Unstable flow and solidification speed due to the interaction of thermocapillary and solutocapillary forces in directional solidification,'' J. Cryst. Growth **166**, 483 (1996).
[8]M. Wanschura, H. C. Kuhlmann, V. M. Shevtsova, and H. J. Rath, ''Thermo- and solutocapillary convection in a cylindrical liquid bridge: Stability of steady axisymmetric flow,'' Adv. Space Res. **16**, 775 (1995).
[9]G. Schmidt, H. Kuhlmann, and H. Rath, ''Instabilities of dynamic thermo- and solutocapillary liquid layers,'' Z. Angew. Math. Mech. **80**, 705 (2000).
[10]T. Campbell, M. Schweizer, P. Dold, A. Cröll, and K. Benz, ''Float-zone growth of $ge_{1-x}si_x$($x \leqslant 10$ at %) single crystals,'' J. Cryst. Growth **226**, 231 (2001).
[11]J. Garandet and T. Alboussière, ''Bridgman growth: Modelling and experiments,'' Prog. Cryst. Growth Charact. Mater. **38**, 73 (1999).
[12]M. Wanschura, V. M. Shevtsova, H. C. Kuhlmann, and H. J. Rath, ''Convective instability mechanisms in thermocapillary liquid bridges,'' Phys. Fluids **7**, 912 (1995).
[13]E. Chénier, C. Delcarte, and G. Labrosse, ''Stability of the axisymmetric buoyant-capillary flows in a laterally heated liquid bridge,'' Phys. Fluids **11**, 527 (1999).
[14]D. Canright, ''Thermocapillary flow near a cold-wall,'' Phys. Fluids **6**, 1415 (1994).
[15]G. Kasperski and G. Labrosse, ''On the numerical treatment of viscous singularities in wall-confined thermocapillary convection,'' Phys. Fluids **12**, 2695 (2000).
[16]G. Chen, A. Lizée, and B. Roux, ''Bifurcation analysis of the thermocapillary convection in cylindrical liquid bridges,'' J. Cryst. Growth **180**, 638 (1997).
[17]E. Anderson, Z. Bai, C. Bischof, S. Blackford, J. Demmel, J. Dongarra, J. D. Croz, A. Greenbaum, S. Hammarling, A. McKenney, and D. Sorensen, *LAPACK Users' Guide*, 3rd ed. (Society for Industrial and Applied Mathematics, Philadelphia, PA, 1999).
[18]T. M. Shih, C. T. Tan, and B. C. Hwang, ''Effects of grid staggering on numerical schemes,'' Int. J. Numer. Methods Fluids **9**, 193 (1989).
[19]R. B. Lehoucq, D. C. Sorensen, and C. Yang, *ARPACK Users' Guide: Solution of Large-Scale Eigenvalue Problems with Implicitly Restarted Arnoldi Methods* (Society for Industrial and Applied Mathematics, Philadelphia, PA, 1998).
[20]J. Leypoldt, H. Kuhlmann, and H. J. Rath, ''Three-dimensional numerical simulation of thermocapillary flows in cylindrical liquid bridges,'' J. Fluid Mech. **414**, 285 (2000).
[21]M. Lappa, R. Savino, and R. Monti, ''Three-dimensional numerical simulation of Marangoni instabilities in liquid bridges: Influence of geometrical aspect ratio,'' Int. J. Numer. Methods Fluids **36**, 53 (2001).